Growth of Sb2Se3 thin films by selenization of RF sputtered binary precursors

Peer-reviewed author version

Shongalova, A; Correia, MR; Teixeira, JP; Leitao, JP; Gonzalez, JC; Ranjbar, S; Garud, S; VERMANG, Bart; Cunha, JMV; Salome, PMP & Fernandes, PA (2018)
Growth of Sb2Se3 thin films by selenization of RF sputtered binary precursors. In: Solar energy materials and solar cells, 187 , p. 219 -226.

DOI: 10.1016/j.solmat.2018.08.003
Handle: http://hdl.handle.net/1942/31489

Growth of Sb_2Se_3 thin films by selenization of RF sputtered binary precursors

A. Shongalova[a,b], M. R. Correia[b], J. P. Teixeira[b], J. P. Leitão[b], J. C. González[c], S. Ranjbar[d], S. Garud[d], B. Vermang[d], J.M.V. Cunha[f], P.M.P. Salomé[b,f], P. A. Fernandes[b,e,f,*]

[a] *Satpayev University, Satpayev street, 22a, 050013 Almaty City, Kazakhstan*
[b] *I3N / Departamento de Física, Universidade de Aveiro, Campus Universitário de Santiago, 3810-193 Aveiro, Portugal*
[c] *Departamento de Física, Universidade Federal de Minas Gerais, 30123-970 Belo Horizonte, Minas Gerais, Brazil*
[d] *IMEC, Kapeldreef 75, 3001 Leuven, Belgium.*
[e] *CIETI / Departamento de Física, Instituto Superior de Engenharia do Porto, Instituto Politécnico do Porto, Rua Dr. António Bernardino de Almeida, 431, 4200-072 Porto, Portugal*
[f] *INL - International Iberian Nanotechnology Laboratory, Av. Mestre José Veiga 4715-330 Braga, Portugal*

Abstract

In this work we present a method to grow Sb_2Se_3 thin films with a potential use as absorber layers in solar cell structures. The films were grown on several substrates: soda-lime glass, Mo coated soda-lime glass and Si . The Sb-Se precursor's films were deposited by RF magnetron sputtering and then selenized under a H_2Se gas flow. Different selenization temperatures were tested and analysed. Compositional and morphological analyses were performed by Energy Dispersive Spectroscopy and Scanning Electron Microscopy, respectively. Phase identification and structural characterization were done by X-ray Diffraction and Raman scattering spectroscopy showing that Sb_2Se_3 is the dominant phase with an orthorhombic crystalline structure. Traces of rhombohedral and amorphous Se secondary phases were also observed supported by their Se-rich compositions. Visible-NIR reflectance measurements allowed to extract a direct bandgap with a value close to 1.06 eV. Photoluminescence spectroscopy shows an emission with a broad band at 0.85 eV for samples selenized at lower temperatures and an intense peak at 0.75 eV for the sample selenized at higher temperatures. Electrical characterization shows low free hole concentrations and mobilities. At low temperatures, the nearest neighbour hopping is the dominant mechanism for the electronic transport for the analysed samples. Both electrical and optical properties are influenced by the type of defects present on samples. A discussion is made on the properties that need to be improved in order that these films can be integrated into thin film solar cells.

Keywords: Sb_2Se_3, thin film, Raman, XRD.

1. Introduction

It is well known that one way of creating an environmentally friendly energy production momentum, which allows mitigating the effects of climate change, is closely linked to the commercial relevance of renewable energy production systems. Photovoltaic (PV) technology can play an important role in this field. Currently dominated by Si-based technology, it has some drawbacks that prevent a greater market presence. High energy payback time, low industrial production rate, and high values of initial investment for a production facilities, among others, are constrains to a higher PV share in the energy production systems in most countries. Due to monolithic integration, lower energy processes and lower material demand, thin film technology presents good arguments to overcome Si technology. CIGS and CdTe based PV cells are currently the most powerful representatives of thin film technology on the market. However, the solar cells based on these materials present problems related to the scarcity and toxicity of some elements that compose them. Alternative materials are currently been studied, such like $Cu_2ZnSn(S,Se)_4$, to be applied as absorber layer in the solar cell structure. But due to its intrinsic complex pentanary structure and restricted growth conditions some difficulties have been encountered. These facts have prevented the production of devices with efficiencies compatible with their commercialization.

Antimony selenide, Sb_2Se_3, is a semiconductor material that belongs to the $A^V_mB^{VI}_n$ group, crystallising in an orthorhombic configuration of the Pnma (62) space group [1]. The first research was published in the 50 s, where Sb_2Se_3, belonging to the same space group of the antimony sulfide, Sb_2S_3, is investigated and structural parameters of Sb_2Se_3 were estimated [2]. Later, this data was confirmed by other research groups [3, 4], as shown in table 1. As a current standard, the crystal lattice parameters for Sb_2Se_3 are taken to be a = 1.16330 nm, b = 1.1700 nm and c = 0.39850 nm.

Over the years, as the interest in Sb_2Se_3 became stronger, researchers devoted to the synthesis of this compound have doubled in the recent decade. Studies revealed that this material

*Corresponding author.
Email addresses: sh.a.k90@mail.ru (A. Shongalova), mrcorreia@ua.pt (M. R. Correia), jenniferpassos@ua.pt (J. P. Teixeira), joaquim.leitao@ua.pt (J. P. Leitão), gonzalez@fisica.ufmg.br (J. C. González), samanehranjbarr@gmail.com (S. Ranjbar), siddhartha.garud@helmholtz-berlin.de (S. Garud), bart.vermang@imec.be (B. Vermang), jose.cunha@inl.int (J.M.V. Cunha), pedro.salome@inl.int (P.M.P. Salomé), paf@isep.ipp.pt (P. A. Fernandes)

lattices param.	ref. [1]	ref. [2]	ref. [3]
a (nm)	1.168	1.171	1.17938
b (nm)	1.158	1.162	1.16478
c (nm)	0.398	0.396	0.39858

Table 1: Comparison of the literature data on the Sb_2Se_3 cell dimensions.

has excellent electrochemical, opto- and thermo-electric properties. Sb_2Se_3 exhibits a direct bandgap between 1.04 - 1.3 eV and optical absorption coefficient higher than 10^5 cm^{-1} in the visible region [5], carrier mobility $\approx$ 10 $cm^2V^{-1}s^{-1}$ for minority carriers and, based on the transient absorption spectroscopy, a carrier lifetime $\approx$ 60 ns [6]. In addition, it has been discovered that Sb_2Se_3 shows an extremely large magnetoresistance [30]. Based on the electrochemical properties, this material has been suggested as an anode material for lithium-ion batteries [8] and hydrogen storage materials [9]. Optoelectronic properties of the material have found applications in optical recording material [10, 11], in thermoelectric devices [12], solar cells and photoelectrochemical cells [13]. At the moment, the best power conversion efficiency value for a Sb_2Se_3 based thin film solar cell with a substrate/FTO/ZnO/Sb_2Se_3/Au structure configuration is 5.93 % [14]. However, theoretically calculated gaps with the ideal Shockley-Queisser value predicted that the efficiency of a solar cells based on Sb_2Se_3 can surpass 30 % [15]. In addition to efficiency of solar cells, the critical parameter for development of such devices is its production cost. Here, Sb_2Se_3 also satisfies necessary criteria as antimony and selenium are widespread and rather cheap elements.

Among Sb_2Se_3 thin-film growth technology, the most common are thermal evaporation [16–20], spin coating [21], chemical bath deposition [22], ionic layer adsorption and reaction methods [23], spray pyrolysis [24], reactive pulsed laser deposition [8], electrodeposition [25, 26], DC magnetron sputtering [29], resistance-heated floating zone furnace [30], just to mention the most used ones.

In this work, we use a method of growing Sb_2Se_3 thin films based on the deposition of Sb-Se precursors by RF-magnetron sputtering followed by an selenization step in a H_2Se gas atmosphere. The films are prepared on different substrates: soda lime glass (SLG), SLG/Mo and Si. We report the effect of the selenization temperatures on the properties of the films. The crystalline structure of the films has been studied by X-ray diffraction and Raman scattering spectroscopy. The characterization of the morphology is done by scanning electron microscopy. Spectrophotometry measurements allowed the study of the optical behaviour of the samples and the determination of the bandgap energies of the compounds. The optoelectronic properties of the samples are also investigated using photoluminescence spectroscopy, Hall effect and electrical resistivity measurements.

2. Experimental Methods

2.1. Preparation of the films

The growth method is based on two steps. The first one refers to the deposition of the binary precursor layer, Sb_xSe_y, by RF magnetron sputtering. The chalcogen incorporation, Se, the composition adjustment and, the selenization process, which allows the crystalline phase formation, are performed in the second stage. In this work we used three types of substrates: 3 × 3 cm^2 soda lime glass (SLG), 2.5 × 2.5 cm^2 Mo coated SLG and 2.5 × 2.5 cm^2 p-Si (100) without removal of the native oxide. The Mo layer thickness is near 350 nm [27]. The samples preparation process begins with the substrate cleaning, with successive ultrasound baths of acetone/alcohol/deionised water. This process ends with the substrate being dried with a N_2 flow. Next, the precursor layers were deposited directly on the different substrates using an Ar atmosphere at an operating pressure of 5×10^{-3} mbar. The Sb_2Se_3 target purity was 99.99%. To avoid target excessive thermal stress or cracking, a low energy density of 0.86 Wcm^2 was used. The precursor film thicknesses of 900 nm was confirmed by contact profilometry described in next section. For the second stage, a rapid thermal furnace system was used. The samples were placed in a susceptor box and submitted to the selenization process depicted in Figure 1. After a quick initial step at 150 °C, the temperature is raised at a rate of 1 °C/s until the maximum temperature is reached. In this work we tested three different maximum temperatures, 300, 350 and 400 °C. This last step has a duration of 900 s. During ramping and fixed-temperature steps a constant H_2Se gas flow at 200 sccm is used as the Se supplier. After this step the H_2Se gas flow is closed and the furnace is subjected to a rapid cooling. During this step the furnace chamber is filled with a mixture of N_2 and H_2.

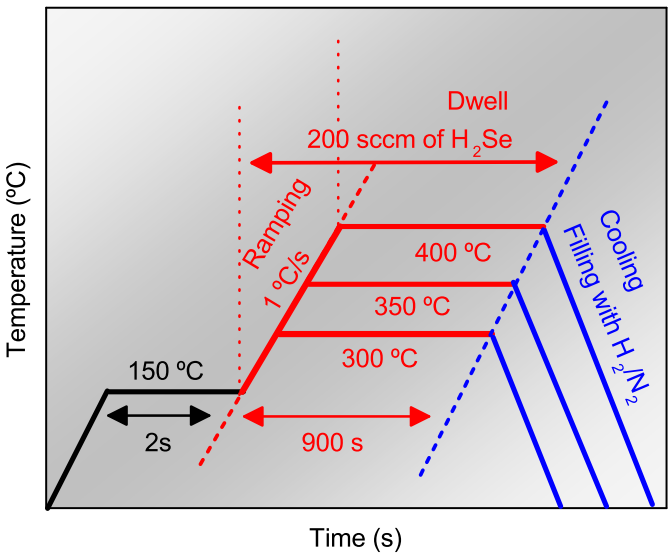

Figure 1: Temperature profiles for the selenization process with three different tested maximum temperatures (300, 350 and 400 °C). The H_2Se gas flux was 200 sccm during the heating ramp and the fixed-temperature step.

2.2. Sample characterization

The composition of the films was analysed by EDS using a Rontec EDS system coupled to a High-resolution NovaNanoSEM 650 SEM system. The accelerating voltage used for the EDS measurements was 30 kV. The same system was used to surface SEM imaging, but with a acceleration voltage of 10 kV. XRD was done in Bragg-Brentano θ-2θ configuration with a PanAnalytical X Pert PRO MRD system with a CuK$_\alpha$ line of 1.5406 Å with the following generator settings: current intensity 40 mA and voltage 45 kV. To measure the precursors' roughnesses and thicknesses a KLA TENCOR P-16+ contact profilometer was used. Raman scattering experiments were carried out at room temperature (RT) using a Jobin-Yvon LabRaman HR800 spectrometer equipped with a multi- 126 channel Peltier cooled (-70 °C) CCD detector, in the backscattering geometry, and using the 632.8 nm excitation line of a HeNe laser. The sample surface was focused with an objective of 50x (N.A=0.50; WD=10.6 mm), and the incident power was varied from 70 μW to 790 μW. The visible-NIR reflectance spectra were recorded at RT, using a dual-beam spectrometer Lambda 950, (Perkin-Elmer) with a 150 mm diameter Spectralon integrating sphere. The photoluminiscence (PL) was measured with the help of a Bruker Vertex 80v Fourier transform infrared spectrometer equipped with an InGaAs detector. The samples were inserted in a He flux cryostat, at 7 K and under He atmosphere. The PL was excited using the 457.9 nm line from a DPSS laser (CVI Melles Griot), non-focused on the sample surface. The excitation power value was 200 mW and measured near the entrance window of the cryostat. The electrical transport properties of the samples deposited in SLG substrates were investigated by Hall effect and electrical resistivity. Ohmic gold contacts were used. Due to the elevated resistivity of the samples, the free hole concentration and mobilities were only determined at 400 K, while the resistivity was measured as a function of temperature.

3. Results and discussion

3.1. Composition and morphology analysis

The sample's composition was analysed by EDS. Table 2 shows the results of the composition ratio of Se over Sb, [Se]/[Sb]. The first row refers to the as-deposited films, *i e*, the precursors samples before the selenization process. All samples are Se poor, with ratio values close to 1.13. These values can be considered the same within the measurement errors. Additional incorporation of chalcogen element is observed after the selenization process. In general, [Se]/[Sb] increases for all temperature profiles and for the three tested substrates. Nevertheless, a substantial difference can be observed when the results of the samples with Si substrate are compared with the SLG and SLG/Mo counterparts. For Si substrates the ratio is close to 1.6 which is close to the stoichiometry value of 1.5. For the other two tested substrates, the amount of detected Se is higher, approximately 1.95. In all cases the selenization temperature does not seem to have a significant effect on the incorporation of additional Se in the films. At least considering the error margin of the EDS and that it is semi-quantitative technique. The fact that Si substrate samples have less Se that the others could be related with its thermal conductivity properties.

Max. Selenization temp.	300 °C	350 °C	400 °C
precursors	1.14	1.12	1.14
Substrate - SLG	1.91	2.12	1.93
Substrate - SLG/Mo	1.95	2.11	1.93
Substrate - Si	1.56	1.61	1.62

Table 2: Composition ratio [Se]/[Sb] for precursors and selenized samples at a maximum temperature of 300 °C, 350 °C and 400 °C with three different substrates: SLG, SLG/Mo and Si.

Surface morphology was investigated using SEM imaging. Figure 2 shows the surface morphology of the precursor layer of the sample selenized at 300 °C on SLG. A regular surface and small grains, with dimensions below 100 nm, can be observed. Figure 3 shows the results for the sample selenized at 300 °C and 400 °C with the three types of substrates. In general, all samples present an increase of the grain size with temperature. This increase can be confirmed by the statistical analysis presented in Figure 4. Based on previous SEM images, a grain contour definition procedure allowed to estimate the grain area and determine the area distribution for each case. As example, shown in Figure 4, samples selenized at 300 °C and 400 °C with SLG/Mo substrates, the peak of the gaussian distribution show a clear trend for higher areas, 0.25 $\rightarrow$ 0.50 μm^2, when the selenization temperature increases. Comparing the results observed in Figure 3 between the three types of substrates, Si ones show a more significant and regular grain increase, which can be related with the thermal properties of this type of substrates allowing for a different thermal budget or with the increased flatness of these substrates compared with SLG and SLG/Mo. Small grains can be observed in the sample selenized at 400 °C with SLG substrate. Localized EDS measurements, confirmed higher Na contents when compared with the average composition, which can be explained by the diffusion of this alkali metal from the SLG substrates [28]. These grains were not observed in the other samples. Sparsely distributed needle-shaped crystallites can be observed in sample with SLG/Mo. Point EDS measurements indicated close to stoichiometric Sb_2Se_3 composition.

3.2. XRD charaterization

The structural analysis was performed using XRD and Raman scattering techniques. As shown in Figure 5, Sb_2Se_3 is the predominant crystalline phase in all the samples. This binary compound has a orthorhombic crystalline structure which belongs to the Pmna (62) space group. The most important reflections occur at 2θ equal to 16.8°, 23.9°, 27.3° and 34.0°, corresponding to the orientation planes (2 0 1), (3 0 1), (3 0 2) and (4 0 2), respectively [31]. For the tested selenization temperatures, this growth method does not seem to follow columnar orientation growth, as published in the literature [20]. For all studied synthesis conditions, the samples follow a planar growth, shown by the (2 0 1) peak intensity when compared

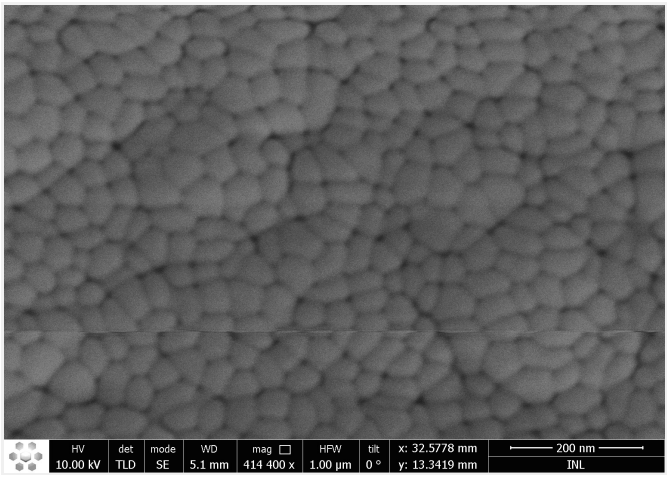

Figure 2: SEM image of a precursor surface sample with SLG substrate.

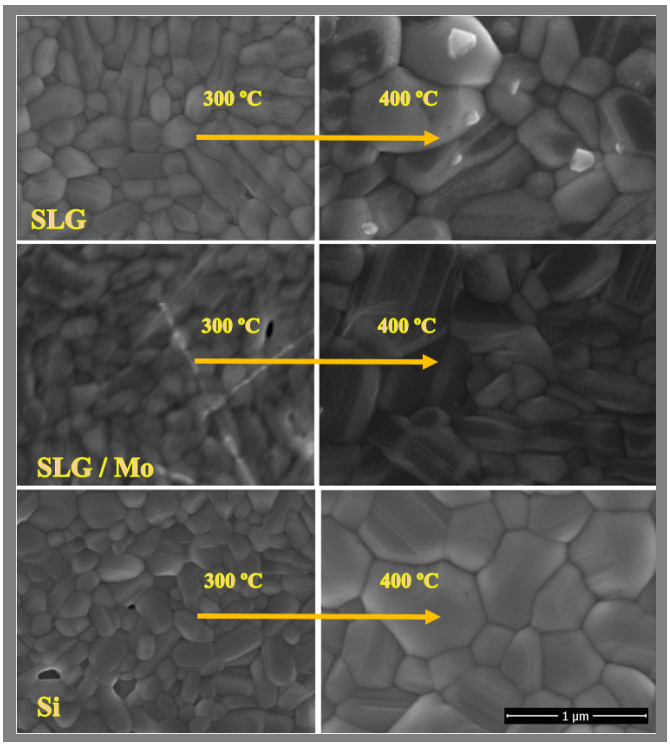

Figure 3: Surface SEM micrographs of the samples selenized at 300 °C and 400 °C with the three types of substrates.

with the powder pattern and the other peaks. In general, the sharpness of the peaks attributed to this phase increase with temperature, meaning that crystallinity increases, as expected. This behaviour is observed for all three substrate types. Reflections from secondary phases, such as Sb and $MoSe_2$, are visible in samples with SLG/Mo substrates. The crystallisation of $MoSe_2$ in a region close to Sb_2Se_3/Mo interface can explain the formation of Sb phase as $MoSe_2$ might deprive Sb of Se. In other systems it has been reported that the chalcogenation of the back contact leads to lack of chalgogen atoms in the absorber layer [32]. Further tests are needed to confirm this statement. The diffractograms shown in Figure 5 from sample with SLG/Mo and Si substrates also present contributions from the substrates layers. For Mo the reflection is located 40.5° and for Si the peaks are at 47.5° and 56.1° according to ICDD database [31]. Some artifacts from the Al sample holder are also visible in these results.

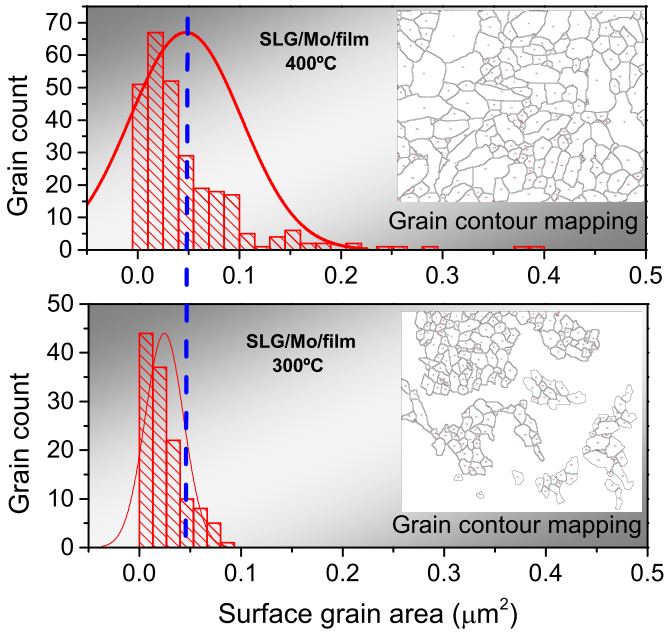

Figure 4: Grain area histogram for the samples selenized at 300 °C and 400 °C with SLG/Mo substrates. Inset plot: Grain contour mapping used for area analysis

It must be highlighted that in literature Sb_2Se_3 space group is commonly identified as Pbnm, where the non-conventional settings cba axis is adopted to define the unit cell. In this work the XRD indexation was done by using the conventional settings abc, whose the space group has the symbol Pnma. Both Pnma and Pbnm are space groups symbols of the orthorhombic system, corresponding to the same symmetry (N° 62), and are related via a simple transformation [33]. The differences are evident when comparing orientation planes previously referred with the ones published [20].

3.3. *Raman scattering results*

Raman scattering characterization of the sample selenized at 300 °C with SLG substrate is shown in Figure 6. Two different spots are presented, corresponding to a) a stoichiometric composition region, and to b) a Se-rich region of the sample. In the first case, the collected Raman spectrum is in agreement with previously reported literature [37]. According to these authors, the most intense peak at 188 cm^{-1} is characteristic of Sb-Se stretching mode and it is pointed as an A_g mode. The peak at 150 cm^{-1} can be associated to Sb-Sb bonds, corresponding to the B_{1g} mode. The vibration modes at 120 and 210 cm^{-1} are related to Se-Se bonds, which are assigned to A_g modes. The graph for Se-rich region show additional features located close to 70, 102, 129, and 252 cm^{-1}, which are assigned to Se with a rhombohedral structure [34]. A small shoulder close to

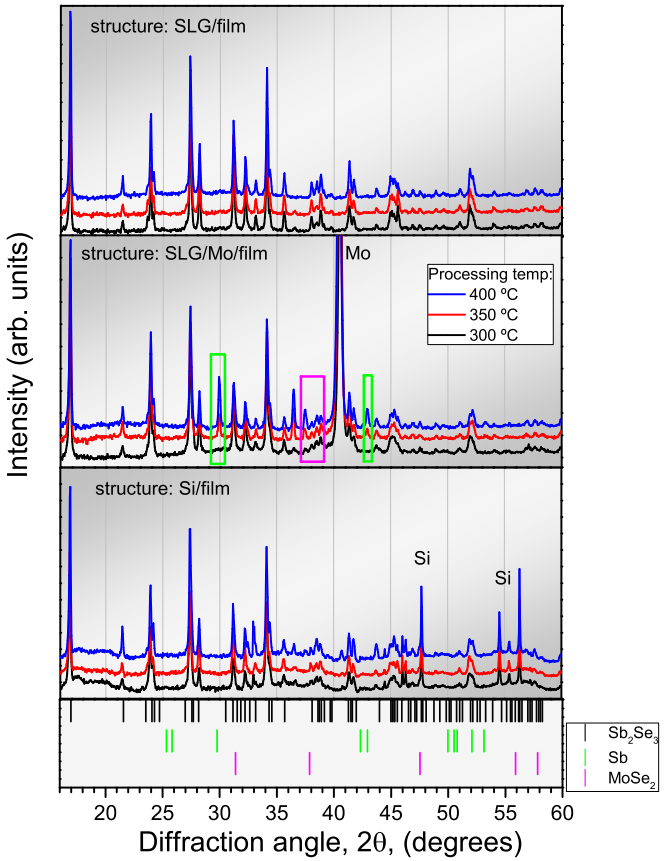

Figure 5: XRD diffractograms of the studied samples with the three different substrate. Blue colored results correspond to maximum selenization temperature of 400 °C, red to 350 °C and black to 300 °C. Colored boxes highlight traces of Sb and $MoSe_2$ crystalline phases for green and magenta colors, respectively. Contributions from the substrates are also visible, such as Mo and Si. Phase assignment was done using the ICDD database [31].

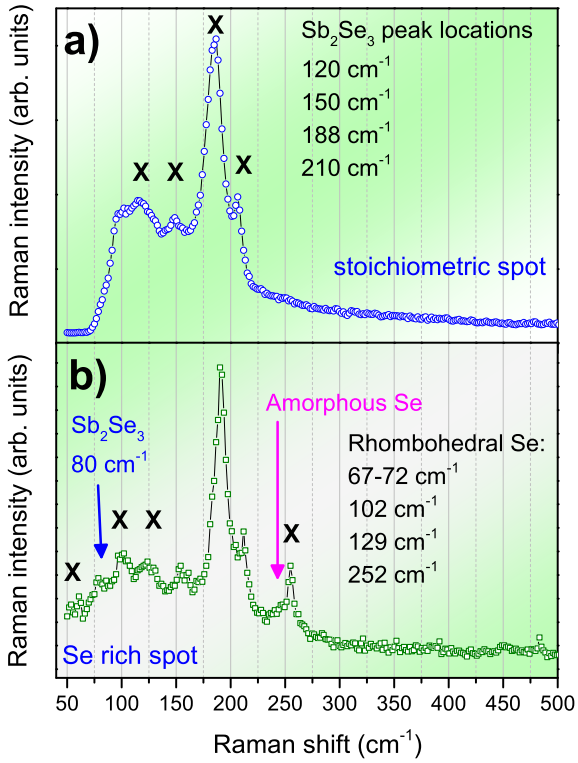

Figure 6: Results of the Raman scattering characterization of the sample selenized at 300 °C with a SLG substrate. Two different spots are shown a) stoichiometric composition where Sb_2Se_3 raman modes are present with the main peaks at 150 and 188 cm^{-1} and b) Se-rich region with additional rhombohedral Se peak signatures according to ref. [34, 37, 38]

the 252 cm^{-1} peak is visible indicating that amorphous Se can also be present in this sample [35]. The power used in these measurements was maintained as low as possible to avoid the sample oxidation. This issue is addressed in more detail elsewhere [38]. When comparing these results with the XRD ones, it is noted that Raman scattering technique can detect Se excess in the composition. Using this characterization technique, small amounts of Se in an amorphous and/or in a crystalline phase can be detected. Although low laser power has been used, it is very likely that part of the detected crystalline Se has been formed during the measurement process. Sparse amorphous and crystalline Se in low quantities are more difficult, if not impossible, to appear in XRD diffractograms. Measurements performed in the other samples did not show relevant differences in the results. Such fact is in accordance with the XRD measurements that show good crystal quality for all films. For the sample with Mo/SLG substrate, we would not expect either the presence of $MoSe_2$ as this phase is located in the rear of the film which is not accessible by the Raman probing volume due to the high light absorption of the Sb_2Se_3 compound [39].

4. Reflectance and Photoluminescence characterization

In Figure 7 it is presented the reflectance spectra of the three samples grown on p-Si substrate. Si was the substrate of choice due to its well known optical properties and due to the increased flatness of the resulting layers which simplifies significantly optical interpretation due to a lesser influence of diffuse properties. The experimental results show that the percentage of reflected light varies from sample to sample. This behaviour can be attributed to the differences in the roughness and the thickness of each sample. By comparing the reflectance spectra of all samples, the shape is found to be similar. Two regions are identified, one between 960-1060 nm and another between 1060-1200 nm, where the reflectance increases abruptly. The first one corresponds to the absorption edge of the silicon substrate and the latter one to the absorption edge of Sb_2Se_3.

To estimate the bandgap in which only the reflection spectra from the film side is measured, we use the approach reported

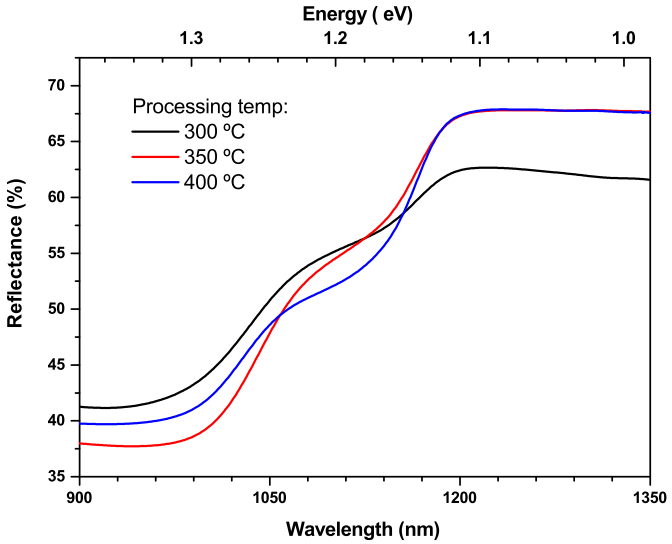

Figure 7: Room Temperature Reflectance spectra of Sb_2Se_3 the films grown on p-Si substrate.

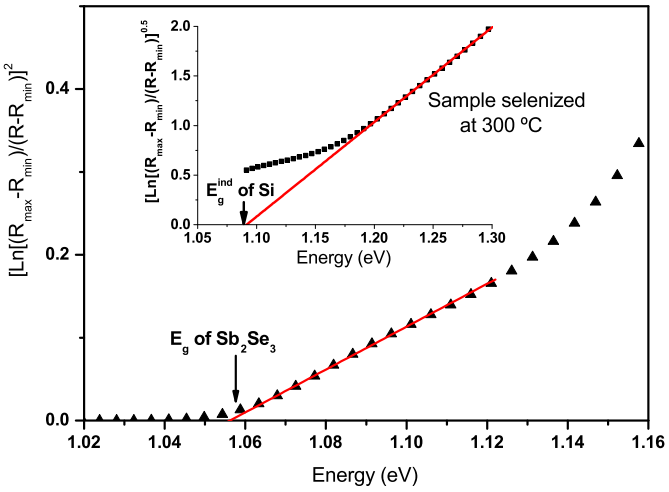

Figure 8: Room Temperature energy bandgap of Sb_2Se_3 film for the sample selenized at 300 °C grown on a p-Si substrate. The inset graph shows the Tauc's plot for the indirect bandgap of Si substrate.

by V. Kumar *et al* [40]. When the thickness is large compared with the wavelength, the absorption coefficient can be related with the reflectance by:

$$2\alpha t = ln(\frac{R_{max} - R_{min}}{R - R_{min}}) \quad (1)$$

where t is the film's thickness, R_{max} and R_{min} are the maximum and the minimum Reflectance in the reflection spectra, respectively and R the reflectance at a given energy ($h\nu$), being h and ν the Planck's constant and the frequency, respectively.

It is well known that the absorption coefficient is proportional to $\propto (h\nu - E_g)^{0.5}$ for a direct gap material and $\propto (h\nu - E_g)^2$ for an indirect gap material [41]. Thus, plotting $[ln(\frac{R_{max}-R_{min}}{R-R_{min}})]^2$ versus $h\nu$ is possible by using Tauc's plot to estimate the direct E_g. In a similar way, plotting $[ln(\frac{R_{max}-R_{min}}{R-R_{min}})]^{0.5}$ versus $h\nu$ allows extracting the indirect E_g.

Both plots were tested and the results have shown that within Sb_2Se_3 absorption spectral range the direct bandgap are well fitted by a straight line as illustrated in Fig. 8 for sample selenized at 300 °C. The Tauc's plots yield to a direct bandgap of 1.06±0.01 eV for this sample. The value obtained is close to the bulk value previously reported [42]. Similar values are extracted for samples selenized at higher temperatures, 1.06±0.03 eV and 1.06±0.06 eV, for 350 °C and 400 °C, respectively. This analysis led to the same value of the bandgap energy for the three samples grown on Si, which agrees with the close stoichiometry values obtained for these samples. Such fact is also in agreement with the XRD and Raman measurements that show both good crystalline quality and the presence of the Sb_2Se_3 phase. It should also be noted that a bandgap around 1 eV, is a value that is compatible with efficient solar cells.

The inset graph of Fig. 8 shows the Tauc's plot for the indirect bandgap within silicon's absorption spectral range of Si substrate of sample processed at 300 °C. As expected, the data are well fitted by a straight line, yielding to an indirect gap of 1.09±0.01 eV. This value is lower than the value of 1.12 eV (300 K), commonly reported for intrinsic bulk silicon [43]. We consider that this difference is a consequence of the bandgap narrowing due to the p doping [44, 45] of the Si substrate used.

Figure 9 a) shows the PL spectra measured at 7 K for the three samples with Si substrate. For all spectra, sharp radiative transitions related with the Si substrate (p-type) are observed, and correspond to free and bound excitons recombinations involving one (TO) or two (TO+O^{Γ}) phonons[46]. An unidentified sharp line at 1.06 eV is also commonly observed in Si [47]. For samples selenized at 300 °C and 350 °C, the luminescence is dominated by a broad and asymmetric band with peak energy at ~0.85 eV and a full width at half maximum (FWHM) of ~100 meV. A shoulder at ~0.75 eV is observed. In the case of sample selenized at 400 °C, this shoulder dominates the spectrum and the relative intensity of the band at ~0.85 eV decreases significantly. This behaviour , along with the large FWHM, suggests a possible relation with defects [47]. On the other hand, the increase of the relative intensity of the band at ~0.75 eV for the highest selenization temperature could reflect a better crystalline quality and increase of the grain size in that film. Additionally, it is observed a decrease of the relative intensity of the Si related sharp lines with the increase of the growth temperature which can be related with a higher thickness of the film and, consequently, a higher absorption of the incident photons in the film. Futhermore, we note that the emissions are in agreement with the estimated bandgap of the films as the luminescence must come from energy values lower than the materials bandgap. The PL measurements were also extended to samples that use SLG as a substrate, which is relevant for the analysis of the electrical measurements described in next section. Figure 9 b) shows the PL spectra for the three different selenization temperatures. For 300 °C, the luminescence is dominated by the band at ~0.85 eV, whereas with the increase of temperature the relative intensity of this

Max. Selenization temp.	300 °C	350 °C	400 °C
p ($\times 10^{13}$ cm^{-3})	9	570	100
μ (cm^{2}v^{-1}s^{-1})	4.5	0.7	4.8
ρ (Ω cm)	15381	1635	1290
N_A (cm^{-3})	—-	1×10^{15}	1.6×10^{19}

Table 3: Electrical characterization results: free hole concentration, p, mobility, μ, resistivity ρ and, acceptor concentration, N_A, measured at 400 K, for the samples deposited in SLG substrates.

band is strongly reduced. For the sample selenized at 350 °C, a shoulder at ∼1.0 eV is observed. In comparison with the luminescence for samples with the Si substrate, the signal-to-noise ratio is lower in the PL spectra measured in the case of SLG substrates. This suggest a possible influence of the substrate on the density of defects in the films. The observation of luminescent is quite important as it is a good indication of good optoelectronic properties relevant to solar cell devices.

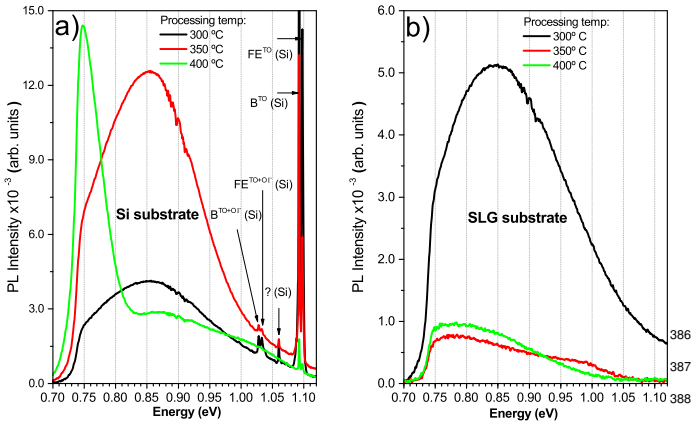

Figure 9: a) PL spectra measured at 7 K for samples with Si substrate selenized at 300 °C, 350 °C and 400 °C , under an excitation of 200 mW. The observed sharp lines are related with the Si substrate. The sharp line at 1.06 eV is an unidentified transition in Si. b) PL spectra measured at 7 K for samples grown on SLG substrates, selenized at 300 °C, 350 °C and 400 °C, under excitation of 200 mW.

5. Electrical characterization

The free hole concentration, p, mobility, μ, and resistivity, ρ, measured at 400 K, for the samples deposited in SLG substrates are reported in table 3. As mentioned, for these measurements, non conductive substrates are needed and SLG was chosen due to is insulating nature.

As shown from these measurements, all samples present low values of carrier concentration and mobility. However, there are not clear correlations between selenization temperature and electrical transport parameters apart from an increase in the free hole concentration by almost two orders of magnitude.

Figure 10 shows the electrical resistivity and all three samples show an Arrhenius behaviour at high temperatures with the same activation energy around 0.5 eV. While in the sample selenized at 400 °C this behaviour appears in the 400 K − 250 K range, for the lowest selenization temperature samples, that range is extended to 170 K. According to the literature, and considering a slow variation of the free carrier mobility with temperature, the activation energy of the resistivity in this region should correspond to $Eg/2$ [48], confirming the values of $Eg \approx 1$ eV above reported. Similar results were already reported for Sb_2Se_3 thin films prepared by thermal evaporation [49] and rapid thermal evaporation [6].

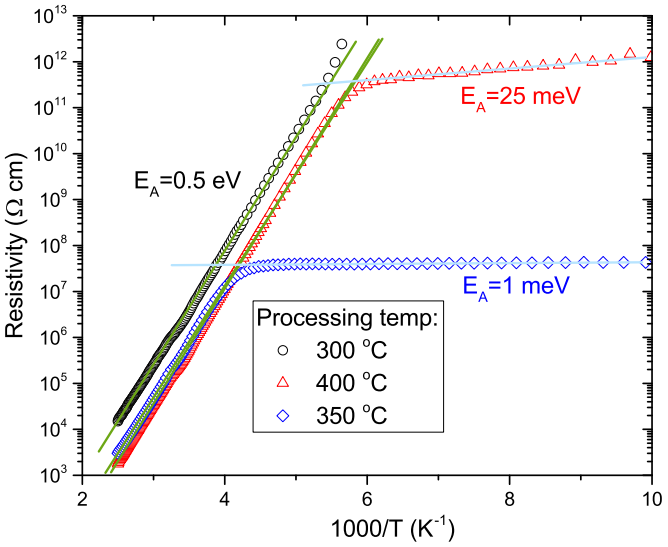

Figure 10: Electrical resistivity as a function of the reciprocal temperatures for the the samples with SLG substractes selenized at 300 °C, 350 °C and 400 °C.

At lower temperatures the slope of the resistivity curve strongly decreases, for the samples selenized at 350 °C and 400 °C , to an activation energy of a few meV. A similar behaviour was also observed for Sb_2Se_3 thin films prepared by rapid thermal evaporation [6]. In reference [6] the resistivity activation energy in this temperature range is associated to shallow acceptors (Se_{Sb}) and Mott variable range hopping ($\rho \approx Exp[(To/T)^{1/4}]$) [50–52]. The expected 1/4 critical exponent of Mott variable range hopping was not observed at low temperatures, instead an Arrhenius dependency with low activation energy was found, see Figure 10. At low temperatures the ionization of shallow acceptors is reduced, as well as the electrical transport by free holes. However, if compensation is present, some of the acceptors and donors in the semiconductor are ionized and holes can hop between spatially fluctuated acceptor levels by emitting or absorbing phonons. Such hopping is more provable between nearest neighbors and this type of charge transport mechanism is called nearest-neighbor hopping (NNH). In order to observe variable range hopping a further decrease in temperature is usually necessary [51, 52]. Both, Arrhenius dependency of the resistivity with temperature and lower thermal activation energy are characteristics of NNH electrical transport [51, 52]:

$$\rho_{\mathrm{NNH}} = \rho_0 \cdot Exp(\frac{E_A}{k_B T}) \tag{2}$$

$$E_A = 0.99 \cdot e^2 \cdot \frac{N_A^{1/3}}{4\pi\epsilon} \tag{3}$$

where ρ_{NNH} is the resistivity of the sample due to NNH, ρ_0 is a constant, N_A is the acceptor concentration, E_A is the activation energy for hole hopping and ϵ, equal to 14.3, is the dielectric permittivity of Sb_2Se_3 [6]. By fitting the experimental data with eq. 2 and using eq. 3 the acceptor concentration in the samples selenized at 350 °C and 400 °C was found and reported in Table 3. Such values of N_A allow for the fabrication of devices like diodes and solar cells. However, depending on the band alignment, higher values of N_A would be required in order to obtain high built-in voltages that allow for high values of open circuit voltages in solar cells. Such increase of doping in chalcopyrite materials is usually obtained by adding alkali elements that change the compensation ratio [28].

At high temperatures the electronic transport is usually dominated by the grain boundaries in polycrystalline semiconductors. Even that the charge carrier mobility is sensible to all defects and scattering mechanism present in the samples, in this context the grain boundary scattering dominates over the rest [51, 53]. Therefore, the increase in the hole mobility value from the 300 °C to the 400 °C sample is probably due to the reduction of the grain potential barrier height accompanied by the increase in grain size, in agreement with SEM observations. PL is also sensitive to several types of defects in semiconductor materials [41]. The observed quenching in the PL measurements (see Figure 9) of the band at 0.85 eV as selenization temperature increases is probably related with the reduction of surface traps at the grain boundaries (particular for the sample selenized at 400 °C). However, other defects should be also involved in the recombination mechanism behind that broad band. Further studies are necessary to deeply understand both, the carrier transport and recombination mechanisms in polycrystalline Sb_2Se_3 samples.

6. Conclusion

In this work, it is shown that a RF magnetron sputtering and subsequent selenization process is suitable to grow Sb_2Se_3 films with good crystal and optoelectronic quality. Some compositional and morphological differences are observed when comparing the films grown on SLG, SLG/Mo and Si substrates. The latter gives compositions close to stoichiometry and more regular grains with increasing selenization temperatures. As expected, a general increase in grain size is observed for all substrates with increasing values of selenization temperature. XRD results show that with this growth method no columnar orientation is observed. Raman scattering detected localized presence of rhombohedral and amorphous Se, which is consistent with the EDS measurements and expected condensation of Se during the cool down of the selenization process. Optical measurements done on the samples with Si substrates allowed us to extract a direct bandgap close to 1.06 eV for the tested selenization temperatures. Photoluminiscence performed in the same samples present a dominant, broad band at ~0.85 eV for samples selenized at 300 °C and 350 °C and, a sharper and intense peak close to 0.75 eV for the sample selenized at 400 °C. An intense peak with an energy close to the bandgap value is a relevant feature in materials for application in solar cells. Electrical characterization of the samples grown on SLG substrates show low free hole concentrations and low mobilities. The study indicates that for low temperature regime the electronic transport is due to nearest-neighbour hopping. The low values obtained for acceptor concentrations pointed out that doping and compensation issues should be addressed in future work.

7. Acknowledgements

This work was funded by FEDER funds through the COMPETE 2020 Programme and National Funds through FCT - Portuguese Foundation for Science and Technology under the projects UID/CTM/50025/2013 and RECI/FIS-NAN/0183/2012 (FCOMP-01-0124-FEDER-027494). M. R. Correia thanks the facilities and technical support provided by CICECO- Aveiro Institute of Materials for the reflectance measurements. P. M. P. Salomé acknowledges the funding of Fundação para Ciência e Tecnologia (FCT) through the project IF/00133/2015. B. Vermang has received funding from the European Research Council (ERC) under the European Union's Horizon 2020 research and innovation programme (grant agreement n° 715027). A. Shongalova acknowledges the funding of Erasmus + program 2016/17. J. C. González acknowledges the support of CAPES, FAPEMIG and CNPq.

References

[1] R. Caracas and, X. Gonze, *First-principles study of the electronic properties of A2B3 minerals, with A = Bi, Sb and B = S, Se*, Physics and chemistry of minerals, 32, 4, 295-300 (2005).

[2] E. Dönges, *Über Chalkogenohalogenide des dreiwertigen Antimons und Wismuts. II. Über Selenohalogenide des dreiwertigen Antimons und Wismuts und über Antimon (III)-selenid Mit 2 Abbildungen*, Zeitschrift für anorganische und allgemeine Chemie, 263, 5-6, 280-291 (1950).

[3] N.W. Tideswell, F. H. Kruse, and J. D. McCullough, *The crystal structure of antimony selenide, Sb_2Se_3*, Acta Crystallographica, 10, 2, 99-102 (1957).

[4] G.P. Voutsas, A.G. Papazoglou, P.J. Rentzeperis, and D. Siapkas, *The crystal structure of antimony selenide, Sb_2Se_3*, Zeitschrift für Kristallographie-Crystalline Materials, 171, 1-4, 261-268 (1985).

[5] Y. Lai, Zhiwei Chen, C. Han, L. Jiang, F. Liu, J. Li, and Y. Liu, *Preparation and characterization of Sb_2Se_3 thin films by electrodeposition and annealing treatment*, Applied Surface Science 261, 510-514 (2012).

[6] C. Chen, D.C. Bobela, Y. Yang, S. Lu, K. Zeng, C. Ge, B. Yang, L. Gao, Y. Zhao, M.C. Beard, and Jiang Tang, *Characterization of basic physical properties of Sb_2Se_3 and its relevance for photovoltaics*, Frontiers of Optoelectronics, 10, 1, 18-30 (2017).

[7] S.-M. Huang, S.-H. Yu, and M. Chou, *Two-carrier transport-induced extremely large magnetoresistance in high mobility Sb_2Se_3*, Journal of Applied Physics, 121, 1, 015107 (2017).

[8] M.-Z. Xue, and Z.-W. Fu, *Pulsed laser deposited Sb_2Se_3 anode for lithium-ion batteries*, Journal of Alloys and Compounds 458, 1, 351-356 (2008).

[9] J. Ma, Y. Wang, Y. Wang, Q. Chen, J. Lian, and W. Zheng, *Controlled synthesis of one-dimensional Sb_2Se_3 nanostructures and their electrochemical properties*, The Journal of Physical Chemistry C, 113, 31, 13588-13592 (2009).

[10] Y. Nakane, N. Sato, H. Makinon, and S. Miyaoka, *Principle of laser recording mechanism by forming an alloy in the multilayer of thin metallic films*, Proc. SPIE 0529, Optical Mass Data Storage I, 76 (1985);

[11] S. Jayakumar, C. Balasubramanian, Sa.K. Narayandass, D. Mangalaraj, and C.P. Girija Vallabhan, *Optical recording characteristics of Sb_2Se_3 thin films using a CW-Ar^+ laser*, Thin Solid Films, 266, 1, 62-68 (1995).

[12] H.C. Kim, T.S. Oh, and D-B. Hyun, *Thermoelectric properties of the p-type Bi_2Te_3-Sb_2Te_3-Sb_2Se_3 alloys fabricated by mechanical alloying and hot pressing*, Journal of Physics and Chemistry of Solids, 61, 5, 743-749 (2000).

[13] B.R. Sankapal, and C.D. Lokhande, *Studies on photoelectrochemical (PEC) cell formed with SILAR deposited Bi_2Se_3-Sb_2Se_3 multilayer thin films*, Solar energy materials and solar cells, 69, 1, 43-52 (2001).

[14] L. Wang, D.-B. Li, K. Li, C. Chen, H.-X. Deng, L. Gao, Y. Zhao, F. Jiang, L. Li, F. Huang, Y. He, H. Song, G. Niu, and J. Tang, *Stable 6%-efficient Sb_2Se_3 solar cells with a ZnO buffer layer*, Nature Energy, 2, 17046 (2017).

[15] W. Shockley, and H.J. Queisser, *Detailed balance limit of efficiency of p-n junction solar cells*, Journal of applied physics, 32, 3, 510-519 (1961).

[16] E.A. El-Sayad, *Compositional dependence of the optical properties of amorphous Sb2Se3-xSx thin films.*, Journal of Non-Crystalline Solids, 354, 32, 3806-3811, (2008).

[17] Z. Li, X. Chen, H. Zhua, J. Chen, Y. Guo, C. Zhang, W. Zhang, X. Niu, Y. Mai, *Sb_2Se_3 thin film solar cells in substrate configuration and the back contact selenization.*" Solar Energy Materials and Solar Cells, 161, 190-196 (2017).

[18] X. Liu, J. Chen, M. Luo, M. Leng, Z. Xia, Y. Zhou, S. Qin, D.-J. Xue, L. Lv, H. Huang, D. Niu, and J. Tang, *Thermal evaporation and characterization of Sb_2Se_3 thin film for substrate Sb_2Se_3/CdS solar cells*, ACS applied materials & interfaces 6, 13, 10687-10695 (2014).

[19] Z. Li, H. Zhu, Y. Guo, X. Niu, X. Chen, C. Zhang, W. Zhang, X. Liang, D. Zhou, J. Chen, and Y. Mai, *Efficiency enhancement of Sb_2Se_3 thin-film solar cells by the co-evaporation of Se and Sb_2Se_3*, Applied Physics Express 9, 5, 052302, (2016).

[20] Y. Zhou, L. Wang, S. Chen, S. Qin, X. Liu, Jie Chen, D.-J. Xue, M. Luo, Y. Cao, Y. Cheng, E. H. Sargent, and J. Tang, *Thin-film Sb_2Se_3 photovoltaics with oriented one-dimensional ribbons and benign grain boundaries*, Nature Photonics 9, 409–415 (2015).

[21] Y.C. Choi, T.N. Mandal, W.S. Yang, Y.H. Lee, S.H. Im, J.H. Noh, and S.I. Seok, *Sb_2Se_3 sensitized inorganic–organic heterojunction solar cells fabricated using a single-source precursor*, Angew. Chem. Int. Ed., 126, 1353–1357 (2014).

[22] Y. Rodríguez-Lazcano, Y. Peña, M.T.S. Nair, and P.K. Nair, *Polycrystalline thin films of antimony selenide via chemical bath deposition and post deposition treatments*, Thin Solid Films, 493, 1, 77-82 (2005).

[23] C.D. Lokhande, B.R. Sankapal, S.D. Sartale, H.M. Pathan, M. Giersig, V. Ganesan, *A novel method for the deposition of nanocrystalline Bi_2Se_3, Sb_2Se_3 and Bi_2Se_3–Sb_2Se_3 thin films—SILAR*, Applied surface science, 182, 3 413-417 (2001).

[24] K.Y. Rajpure, and C.H. Bhosale, *Effect of Se source on properties of spray deposited Sb_2Se_3 thin films*, Materials chemistry and physics 62, 2 169-174 (2000).

[25] A.P. Torane, and C.H. Bhosale, *Preparation and characterization of electrodeposited Sb_2Se_3 thin films from non-aqueous media*, Journal of Physics and Chemistry of Solids 63, 10 1849-1855 (2002).

[26] A.M. Fernandez, and M.G. Merino, *Preparation and characterization of Sb_2Se_3 thin films prepared by electrodeposition for photovoltaic applications*, Thin Solid Films 366, 1 202-206 (2000).

[27] P.M.P. Salomé, J. Malaquias, P. A. Fernandes and A. F. da Cunha, *Mo bilayer for thin film photovoltaics revisited*, J. Phys. D: Appl. Phys. 43, 345501 (7pp) (2010).

[28] P.M.P. Salomé, H.Rodriguez-Alvarez and S.Sadewasser, *Incorporation of alkali metals in chalcogenide solar cells*, Solar Energy Materials and Solar Cells, 143, 9-20 (2015).

[29] C. Yuan, L. Zhang, W. Liu, and C. Zhu, *Rapid thermal process to fabricate Sb_2Se_3 thin film for solar cell application*, Solar Energy 137, 256-260 (2016).

[30] S.M. Huang, S.H. Yu, and M. Chou, *Two-carrier transport-induced extremely large magnetoresistance in high mobility Sb_2Se_3*, Journal of Applied Physics 121, 1, 015107 (2017).

[31] International Centre for Diffraction Data—Reference Code, 01-072-1184 (Pbnm (62) Sb_2Se_3), 04-004-5993 (Pnma (62) Sb_2Se_3), 96-901-3396 (Sb), 01-071-4645 (Mo), and 09-0312 (MoS_2).

[32] J. J. Scragg, J. T. Wätjen, M. Edoff, T. Ericson, T. Kubart, and C. Platzer-Björkman, *A Detrimental Reaction at the Molybdenum Back Contact in $Cu_2ZnSn(S,Se)_4$ Thin-Film Solar Cells*, J. Am. Chem. Soc. 134, (47), pp 19330–19333, (2012)

[33] B.B. Van Aken, PhD Thesis Rijksuniversiteit Groningen (1973).

[34] K. Nagata, K. Ishibashi, and Y. Miyamoto, *Raman and infrared spectra of rhombohedral selenium*, Jpn. J. Appl. Phys. , 20, 3, 463-469 (1981).

[35] P. M. P. Salomé, P. A. Fernandes, J. P. Leitão, M. G. Sousa, J. P. Teixeira and A. F. da Cunha, *Secondary crystalline phases identification in Cu2ZnSnSe4 thin films: contributions from Raman scattering and photoluminescence*, J Mater Sci 49: 7425 (2014) .

[36] Y. Zhou, M. Leng, Z. Xia, J. Zhong, H. Song, X. Liu, B. Yang, J. Zhang, J. Chen, K. Zhou, J. Han, Y. Cheng, and J. Tang, *Solution-Processed Antimony Selenide Heterojunction Solar Cells*, Adv. Energy Mater. 2014, 1301846

[37] Z.G. Ivanova, E. Cernoskova, V.S. Vassilev, S.V. Boycheva, *Thermomechanical and structural characterization of $GeSe_2$-Sb_2Se_3-ZnSe glasses*, Materials Letters 57 (2003) 1025.1028.

[38] A. Shongalova, M. R. Correia, B. Vermang, J.M.V. Cunha, P.M.P. Salomé and P.A. Fernandes, *On the identification of Sb_2Se_3 using Raman scattering*, MRS Communications, Materials Research Society, 1-6,(2018).

[39] P.A. Fernandes, P.M.P. Salomé, A.F. Sartori, J. Malaquias, A.F. da Cunha , Björn-Arvid Schubert, J.C. González, G.M. Ribeiro, *Effects of sulphurization time on Cu_2ZnSnS_4 absorbers and thin films solar cells obtained from metallic precursors*, Solar Energy Materials & Solar Cells 115 157–165 (2013).

[40] V. Kumar, S. K. Sharma, T.P. Sharma and, V. Singh, *Band gap determination in thick films from reflectance measurements*, Optical materials, 12(1), 115-119 (1999).

[41] J.I. Pankove, *Optical Processes in Semiconductors*, Dover, New York, (1971).

[42] O. Madelung, *Semiconductors, Other than Group IV Elements and III+V Compounds*, Springer-Verlag, Germany, (1992).

[43] M. Fox, *Optical properties of solids*, Oxford master series in condensed matter physics, 76-78, (2001).

[44] A. Schenk, *Finite-temperature full random-phase approximation model of band gap narrowing for silicon device simulation*, Journal of Applied Physics, 84 (7), 3684–3695, (1998).

[45] D. Yan and, and A. Cuevas, *Empirical determination of the energy band gap narrowing in p+ silicon heavily doped with boron*, Journal of Applied Physics 116, 19, 194505, (2014).

[46] M.A. Vouk, and E.C. Lightowlers, *Two-phonon assisted free exciton recombination radiation from intrinsic silicon*, Journal of Physics C: Solid State Physics 10, 3689 (1977).

[47] N.M. Santos, B.P. Falcão, J.P. Leitão, N.A. Sobolev, M.C. Carmo, N.S. Stepina, A. Yakimov, and A.I. Nikiforov, *Optical study of strained double GeSi quantum dot layers*, IOP Conference Series: Materials Science and Engineering 6, 012018 (2009).

[48] G. I. Yepifanov, and Yu A. Moma, *Introduction to Solid State Elctronics*, p 232. Mir, Moscow (1984).

[49] F. Abd El-Salam, M. A. Afifi, E. Abd El-Wahabb, Electrical resistivity of crystalline Sb_2Se_3, Vacuum 44, pp 111-116 (1993).

[50] N. Cifuentes, H. Limborço, E.R. Viana, D.B. Roa, A. Abelenda, M.I.N. da Silva, M.V.B. Moreira, G.M. Ribeiro, A.G. de Oliveira, and J.C. González, *Electronic transport in p-type Mg-doped GaAs nanowires*, Physica Status Solidi B: Basic Solid State Physics 253, pp 1960-1964 (2016).

[51] J.C. González, G.M. Ribeiro, E.R. Viana, P.A. Fernandes, P.M.P. Salomé, K. Gutiérrez, A. Abelenda, F.M. Matinaga, J.P. Leitão, and A.F. da Cunha, *Hopping conduction and persistent photoconductivity in Cu_2ZnSnS_4 thin films*, J. Phys. D: Appl. Phys. 46 155107 (2013).

[52] E.R. Viana, J.C. González, G.M. Ribeiro, and A.G. de Oliveira, *3D hopping conduction in SnO2 nanobelts*, Physica Satus Solidi-rapid research letters, 6, pp 262-264 (2012).

[53] J.C. González, P.A. Fernandes, G.M. Ribeiro, A. Abelenda, E.R. Viana, P.M.P. Salomé, A.F. da Cunha, *Influence of the sulphurization time on the morphological, chemical,structural and electrical properties of Cu_2ZnSnS_4 polycrystalline thin films*, Solar Energy Materials and Solar Cells 123,58–64 (2014).